Joint Self-Supervised Image-Volume Representation Learning with Intra-inter Contrastive Clustering

Duy M. H. Nguyen^{1,10*}, Hoang Nguyen², Truong T. N. Mai³, Tri Cao², Binh T. Nguyen² Nhat Ho⁴, Paul Swoboda⁵, Shadi Albarqouni ^{6,7}, Pengtao Xie⁸, Daniel Sonntag^{9,10}

¹Department of Computer Science, University of Stuttgart, Germany

²AISIA Lab, University of Science - VNU HCM, Vietnam

³Department of Multimedia Engineering, Dongguk University, South Korea

⁴Department of Statistics and Data Sciences, University of Texas at Austin, United States

⁵Max Planck Institute for Informatics, Germany

⁶Helmholtz AI, Helmholtz Munich, Germany

⁷Clinic for Diagnostic and Interventional Radiology, University of Bonn, Germany

⁸Department of Electrical and Computer Engineering, University of California San Diego, United States

⁹Department of Computer Science, Oldenburg University, Germany

¹⁰German Research Center for Artificial Intelligence, Germany

*ho_minh_duy.nguyen@dfki.de

Abstract

Collecting large-scale medical datasets with fully annotated samples for training of deep networks is prohibitively expensive, especially for 3D volume data. Recent breakthroughs in self-supervised learning (SSL) offer the ability to overcome the lack of labeled training samples by learning feature representations from unlabeled data. However, most current SSL techniques in the medical field have been designed for either 2D images or 3D volumes. In practice, this restricts the capability to fully leverage unlabeled data from numerous sources, which may include both 2D and 3D data. Additionally, the use of these pre-trained networks is constrained to downstream tasks with compatible data dimensions. In this paper, we propose a novel framework for unsupervised joint learning on 2D and 3D data modalities. Given a set of 2D images or 2D slices extracted from 3D volumes, we construct an SSL task based on a 2D contrastive clustering problem for distinct classes. The 3D volumes are exploited by computing vectored embedding at each slice and then assembling a holistic feature through deformable self-attention mechanisms in Transformer, allowing incorporating long-range dependencies between slices inside 3D volumes. These holistic features are further utilized to define a novel 3D clustering agreement-based SSL task and masking embedding prediction inspired by pre-trained language models. Experiments on downstream tasks, such as 3D brain segmentation, lung nodule detection, 3D heart structures segmentation, and abnormal chest X-ray detection, demonstrate the effectiveness of our joint 2D and 3D SSL approach. We improve plain 2D Deep-ClusterV2 and SwAV by a significant margin and also surpass various modern 2D and 3D SSL approaches.

Introduction

Creating large-scale medical image datasets for training neural networks is a major obstacle due to the complexity of

*Corresponding author.

Copyright © 2023, Association for the Advancement of Artificial Intelligence (www.aaai.org). All rights reserved.

data acquisition, expensive annotations, and privacy concerns (Cheplygina, de Bruijne, and Pluim 2019; Kaissis et al. 2020). To alleviate these challenges, a conventional approach is to train deep networks, e.g., ResNet-50 (He et al. 2016), on large-scale natural image datasets such as ImageNet (Deng et al. 2009) and subsequently fine-tune them on the target medical domain. However, such schemes are suboptimal due to the large domain discrepancy between natural images and medical data (Raghu et al. 2019; Nguyen et al. 2022b). This has motivated other techniques for collecting annotated medical datasets across domains and training networks using full (Gibson et al. 2018; Chen, Ma, and Zheng 2019) or semi-supervision (Wang et al. 2020). Nevertheless, the amount of acquired relevant training data in this manner is still limited, which significantly limits the performance of deep neural networks.

Self-supervised learning (SSL) has recently emerged as a new trend in medical imaging due to its ability in obtaining feature representations from unlabeled data by solving proxy tasks, which can be broadly categorized into *generative* (Chen et al. 2019) and *discriminative* ones (Chen et al. 2020a; He et al. 2020). Discriminative SSL can be further separated into three directions: instance level-based methods (Zbontar et al. 2021; Caron et al. 2021), contrastive learning-based methods (He et al. 2020; Chen, Xie, and He 2021) and clustering-based methods (Caron et al. 2020; Li et al. 2021). Depending on a specific 2D, e.g., X-ray images or 3D magnetic resonance imaging (MRI) application, variations of these methods can be modified using 3D convolutional neural networks (CNNs) or Transformer architectures (Taleb et al. 2020; Haghighi et al. 2021; Tang et al. 2022).

However, all aforementioned SSL methods have been designed to learn on either 2D or 3D data modalities. As a result, they suffer from two major limitations. First, the ability to exploit unlabeled data from multiple source domains, which commonly occurs in medical data, is restricted. For

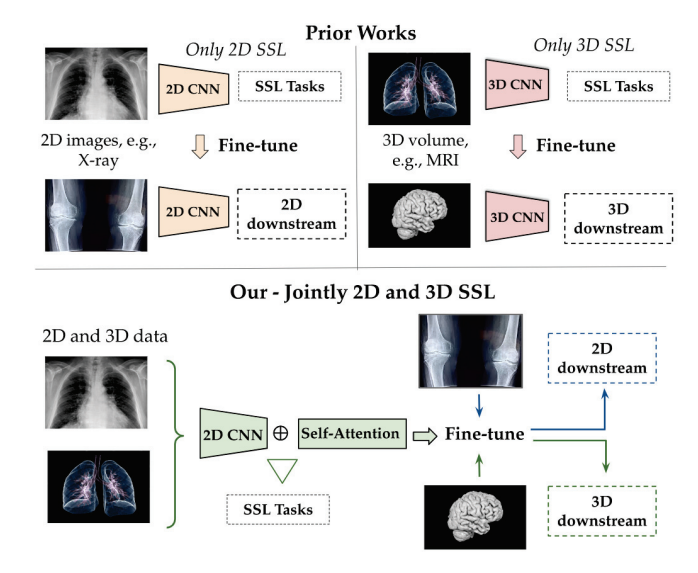


Figure 1: The main distinctions between our work and prior studies on 2D and 3D SSL. We can learn representations from diverse data and the pre-trained weights can be transferred for both 2D and 3D downstream tasks.

instance, 3D CNN-based SSL methods can not use X-ray, digital retinal, and dermoscopic images taken from lung, eye retina, and skin lesions, respectively. Although 2D CNN-based SSL methods can process 3D volumes slice-by-slice along a specific plane (either sagittal, coronal, or horizontal) (Nguyen et al. 2022a; Jun et al. 2021), these approaches do not capture long-range inter-slice correlations and thus may result in inferior performance in 3D applications. Second, using a pure 2D or 3D strategy limits the fine-tuning phase since the pre-trained models are only applicable for down-stream tasks with the same dimensionality. For instance, pre-trained 3D-CNN cannot handle object detection (Nguyen et al. 2021, 2022c), while pre-trained 2D-CNN might not be usable for 3D classification tasks (Table 3, third column).

In this work, we propose a novel technique to overcome those barriers by presenting a hybrid SSL architecture harnessing both 2D and 3D medical data. The method has the following properties. First, it is built on top of cutting-edge 2D SSL baselines while reserving designed CNN architecture, benefiting from the latest advancements of SSL in natural images. Second, when applied to 3D data, we formulate both intra-dependencies inside slices and long-range interdependencies across slices, resulting in more complex contrastive cues that force the network to seek associated local and global feature representations.

Specifically, we compose a joint image-volume representation learning comprising a 2D CNN (ResNet-50) to extract feature embedding at the image level and a deformable attention transformer (Zhu et al. 2020; Liu et al. 2021; Xia et al. 2022) to express correlations among local slices, aiming to derive a holistic representation at the 3D volume level. Unlike standard attentions in Transformer (Vaswani et al. 2017; Dosovitskiy et al. 2020) which treat all attention po-

sitions equally, our deformable mechanism pays attention to only a flexible small set of major slices conditioned on input data. This largely reduces computational complexity and permits handling the multi-scale feature maps which are desired properties in medical downstream tasks.

The proposed method is trained on SSL tasks utilizing both current 2D SSL methodologies and our two novel 3D pre-text tasks. To this end, we employ two state-of-the-art contrastive clustering-based SSL approaches, Deep-Cluster-V2 (Caron et al. 2018) and SwAV (Caron et al. 2020). With each baseline, we first perform the relevant 2D proxy tasks based on an agreement clustering for 2D slices taken from 3D volumes. We next compute multi-level features at each slice within a 3D volume encoded with their positions and feed them into the deformable transformer. The global embedded features derived from this transformer are employed to define an agreement clustering for 3D volumes and a masked encoding feature prediction motivated by the success of the language model BERT (Devlin et al. 2018). By optimizing these conditions, intuitively we are able to learn feature extractors at the local- and global-level in a constraint manner, resulting in consistent cues and improved performance in downstream tasks. Furthermore, the pre-trained networks are adaptable with data dimensional compatibility by employing the 2D CNN for 2D tasks or the hybrid 2D CNN- Transformer architectures for 3D tasks.

In summary, we make the following contributions. First, we present an SSL framework capable of using various data dimensions and producing versatile pre-trained weights for both 2D and 3D downstream applications (Figure 1). Second, we introduce the deformable self-attention mechanisms which utilize multi-level feature maps and capture flexible correlations between 2D slices, resulting in a powerful global feature representation. On top of this, we developed the novel 3D agreement clustering extended from the earlier 2D clustering problem as well as proposed the masking embedding prediction. Finally, extensive experiments on public benchmarks confirmed that we improve state-of-the-art 2D baselines and surpass several latest SSL competitors based on CNN or Transformer.

Related Work

Self-supervised Learning in Medical Image Analysis Our work is closely related to instance-based constrative learning and unsupervised contrastive clustering. The instance-based contrastive methods seek an embedding space where transformed samples, e.g., crops, drawn from the same instance, e.g., image, are pulled closer, and samples from distinct instances are pushed far away. The contrastive loss is constructed based on positive and negative feature pairs generated by various approaches, such as memory bank (Wu et al. 2018), end-to-end (Chen et al. 2020a), or momentum encoder (Chen, Xie, and He 2021). Despite achieving good performance in various settings, the instance-based method has crucial limitations in requiring a large negative batch size and choosing hard enough negative ones. The unsupervised contrastive clustering (Caron et al. 2018, 2020) in other directions tries to learn representations based on groups of images with similar features rather than

individual instances. For instance, SwAV (Caron et al. 2020) simultaneously clusters the data while imposing consistency between cluster assignments generated for distinct augmentations of the same image. Currently, extensions on this direction have considered latent variables of centre points (Li et al. 2021), multi-view clustering (Pan and Kang 2021), or mutual information (Do, Tran, and Venkatesh 2021).

In medical image analysis, several SSL methods have designed pre-text tasks based on 3D volume's properties such as reconstructing spatial context (Zhuang et al. 2019), random permutation prediction (Chen et al. 2019), selfdiscovery and self-restoration (Zhou et al. 2021b; Haghighi et al. 2021). Some other efforts attempted to develop 3D CNN architecture while retaining defined SSL tasks on 2D CNN (Taleb et al. 2020). Another line of research considered the cross-domain training with two or more datasets, aiming to derive a generic invariant pre-trained model (Zhang et al. 2020). Besides, existing methods also exploit the domain- and problem-specific cues such as structural similarity across 3D volumes in order to define global and local contrastive losses (Chaitanya et al. 2020; Xie et al. 2020). However, most of these techniques have only been applied to 2D or 3D data, which are different from ours in terms of data usage and flexible pre-trained weights in downstream tasks (Figure 1).

SSL Transformer in Medical Imaging Vision transformers, adapted from sequence-to-sequence modeling in natural language processing, are initially used in image classification tasks (Dosovitskiy et al. 2020). In the context of SSL, 2D transformer-based methods such as Moco-v3 (Chen, Xie, and He 2021) and DINO (Caron et al. 2021) are also introduced and achieved promising performance. To elaborate 3D volumes, Tang et al. (2022) introduced a 3D transformer-based model comprising a Swin Transformer encoder (Liu et al. 2021) and skip connections. Likewise, Xie et al. (2021) adapted a mixed 2D-3D Pyramid Vision Transformer architecture (Wang et al. 2021) to learn rich representations from diverse data.

Compared with prior works in SSL (Caron et al. 2021; Tang et al. 2022), we employ Transformer to define the interaction between 2D slices inside a 3D volume rather than a fixed 2D or 3D network backbone, allowing us to adapt to varied data dimension downstream applications. Furthermore, we the first adapt deformable attention mechanism (Zhu et al. 2020; Liu et al. 2021; Xia et al. 2022) for SSL, which currently are only validated performance in supervised learning. Xie et al. (2021) shares the same ideas with us in jointly learning diverse unlabeled data; however, this method designs a specific SSL task while our 3D loss is extended directly from standard 2D cases. Also, we achieve similar or better performance compared with this baseline while using a smaller amount of unlabeled data.

Methodology

Our approach is built on top of 2D contrastive clustering learning baselines including Deep-ClusterV2 (Caron et al. 2018) and SwAV (Caron et al. 2020). Both approaches rely on clustering together features produced by neural net-

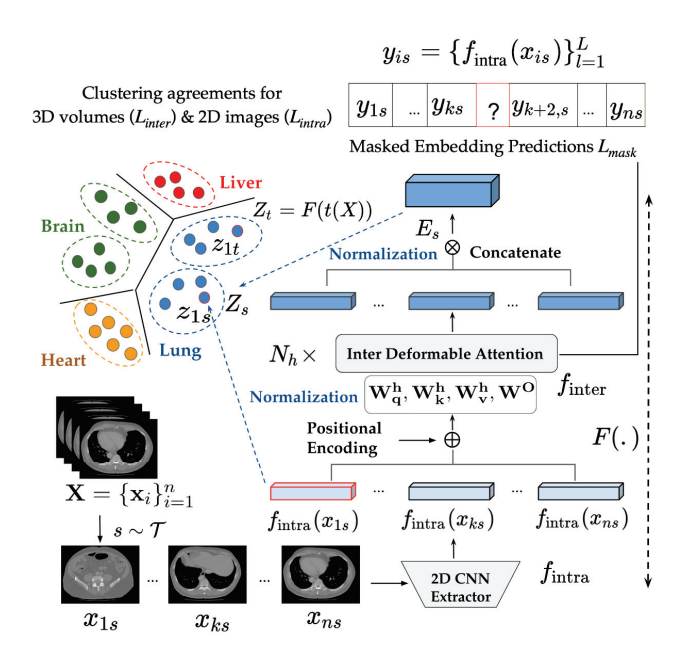


Figure 2: Overview of our joint SSL image-volume framework. Given a 3D volume ${\bf X}$ and a random transformation s, we compute the embedding feature for each slice using a 2D-CNN extractor $f_{\rm intra}$ and produce a global feature Z_s through the Inter Deformable Attention $f_{\rm inter}$. Similarly, corresponding features can be derived from 2D and 3D augmented views of ${\bf X}$ by another transformation t. Through cluster agreement losses for 2D slices ($L_{\rm intra}$), e.g. between z_{1s} and z_{1t} , and for 3D volumes between z_s and z_t (L_{inter}), feature representations can be learned. Additionally, we employ a masked feature embedding prediction given 2D slices' embedding outputs as an SSL task to capture data's long-term interdependence.

work backbones. Deep-ClusterV2 forces each cluster to have roughly the same size. SwAV additionally imposes losses on assigning augmentations of an image into the same cluster. Below, we recapitulate the SwAV baseline and then show how it can be extended through the deformable self-attention (Zhu et al. 2020; Xia et al. 2022) to 3D volumes. Additionally, we introduce a new proxy task based on missing embedding prediction in order to make the designed architecture be stable under perturbations. An illustration of our approach can be seen in Figure 2. A variation of our method using DeepCluster-V2 can be derived analogously.

Notation: We assume to be given K unlabeled datasets $\mathbb{D}=\{D_1,D_2,...,D_K\}$ consisting of instances $D_i=\{\mathbf{X_1},\,\mathbf{X_2},...,\mathbf{X_{m_i}}\}, i\in[1,\,K]$, which include $\mathbf{m_i}$ 2D or 3D volumes $\mathbf{X_j},\,\mathbf{j}\in[1,\mathbf{m_i}]$. Given a particular dataset $D\in\mathbb{D}$, we assume that each 3D volume contains n slices, i.e. $\forall\,\mathbf{X}\in D,\,\mathbf{X}=\{\mathbf{x}_i\}_{i=1}^n.$

Clustering Agreement for 2D Images

SwAV uses a proxy task for a "swapped" prediction problem in which the cluster assignment of a transformed image is to be found from the feature representation of another transformation of the same image and vice versa. In our framework, we refer to this proxy task as an *intra-dependence* correlation since it learns only from 2D slices inside a 3D volume without taking into account correlations between different slices of the same volume. Below we formally specify the intra-dependence correlation.

Let f_{intra} be a CNN, e.g., ResNet-50 (He et al. 2016), extracting feature embeddings for each 2D slice $\mathbf{x}_i \in \mathbf{X}$. The cluster assignment matrix $\mathbf{C} = [c_1, \dots, c_H]$ has columns c_j , each column corresponding to the feature representation of the j-th cluster, and H is the number of hidden clusters. Given a 2D slice $\mathbf{x}_i \in \mathbf{X}$, we choose randomly two transformations $s, t \in T$, where T is a set of pre-defined image transformations. We apply s and t on \mathbf{x}_i and obtain two augmented views \mathbf{x}_{is} , \mathbf{x}_{it} . Using f_{intra} and normalization gives us the respective features \mathbf{z}_{it} and \mathbf{z}_{is} (Figure 2), i.e.

$$\mathbf{z_{ik}} = f_{\text{intra}}(\mathbf{x}_{ik}) / ||f_{\text{intra}}(\mathbf{x}_{ik})||_2, \ k \in \{s, t\}.$$
 (1)

These features are then used to find corresponding cluster assignments \mathbf{q}_{it} , \mathbf{q}_{is} , i.e., the probability distribution over all clusters, called codes in SwAV. To find these codes, we sample a batch of size B from slices of volumes coming from all datasets and optimize

$$\max_{\mathbf{Q} \in \mathbb{O}} \mathbf{Tr}(\mathbf{Q}^T \mathbf{C}^T \mathbf{Z}) + \epsilon H(\mathbf{Q}), \tag{2}$$

where $\mathbf{Z} = [\mathbf{z}_1,...,\mathbf{z}_{2B}]$ is formed by adding features z_{it}, z_{is} of each x_i in the batch B, the assignment matrix is $\mathbf{Q} = [\mathbf{q}_1, \ldots, \mathbf{q}_{2B}]$ and $\mathbb{Q} = \{\mathbf{Q} \in \mathbb{R}_+^{K \times B} : \mathbf{Q} \mathbb{1}_B = \frac{1}{K} \mathbb{1}_K, \mathbf{Q} \mathbb{1}_K = \frac{1}{B} \mathbb{1}_B \}$ is the set of all possible assignment matrices such that slices are assigned on average uniformly, H is the entropy function and ϵ is a hyper-parameter that controls the smoothness of the mapping. Since views coming from the same sample \mathbf{x}_i should have features that are assigned to the same cluster, we formulate the intradependency code prediction loss

$$L_{\text{intra}}(\mathbf{z}_{it}, \mathbf{q}_{it}, \mathbf{z}_{is}, \mathbf{q}_{is}) = l(\mathbf{z}_{it}, \mathbf{q}_{is}) + l(\mathbf{z}_{is}, \mathbf{q}_{it})$$
(3)

where the function $l(\mathbf{z}, \mathbf{q})$ quantifies the fit between feature \mathbf{z} and code assignment \mathbf{q} defined as

$$l(\mathbf{z}_t, \mathbf{q}_s) = -\sum_k \mathbf{q}_s^k \log \mathbf{p}_t^k, \text{ where } \mathbf{p}_t^k = \frac{\exp(\frac{1}{\tau} \mathbf{z}_t^T \mathbf{c}_k)}{\sum_{k'} \exp(\frac{1}{\tau} \mathbf{z}_t^T \mathbf{c}_{k'})}$$
(4)

Here τ is a hyper-parameter.

Intuitively, if two features encode views coming from the same slice, the loss $l(\mathbf{z}_t, \mathbf{q}_s)$ in Eq. (4) encourages their predicted clusters should be identical. Finally, by optimizing Eq. (3) over $\mathbf{x}_i \in \mathbf{X}$ we can learn feature representations f_{intra} and centroids \mathbf{C} by minimizing

$$L_{2D} = \min_{f_{\text{intra}}, \mathbf{C}} E_{\mathbf{x}_i \in \mathbf{X}} \left[L_{\text{intra}}(\mathbf{z}_{it}, \mathbf{q}_{it}, \mathbf{z}_{is}, \mathbf{q}_{is}) \right], \ s, t \sim T.$$
(5)

Clustering Agreement for 3D Volumes with Inter Deformable Attention

In the presence of both unlabeled 2D and 3D data, we argue that the clustering agreement constraint in Eq.(4) should also hold for feature representations of *different views of the*

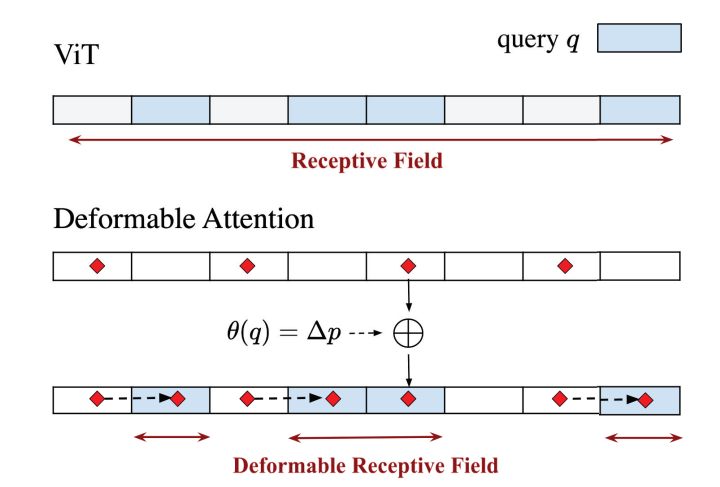


Figure 3: Comparison of Deformable Attention (DAT) with standard Vision Transformer (ViT) in our setting using slice's embedding vector. Given a query q, ViT pays attention to all possible positions including possibly less relevant feature maps while DAT learns important regions based on grid points (red points) and their shifted vectors using offsets Δp predicted by $\theta(q)$.

3D volume (Figure 2). We call this agreement as an inter-dependence correlation. It forces the feature representation to additionally consider long-range interactions among 2D slices inside a 3D volume (Eq.(10)). To this end, we adapt the Transformer to aggregate local features computed by $f_{\rm intra}$ at each slice to form a holistic feature representation for a 3D volume. However the standard attention mechanisms in vanilla Transformer such as ViT (Dosovitskiy et al. 2020) does not fit well in our setting when it permits excessive number of keys to contribute per query patch. As a result, the required memory and computational costs increase significantly as well as features can be influenced by irrelevant parts.

To mitigate these problems, we use the deformable selfattention mechanism which is recently introduced in supervised learning such as object detection and image classification (Zhu et al. 2020; Xia et al. 2022). Generally this strategy seeks important positions of keys and value pairs in self-attention in a dependent-way rather than a fixed window size as ViT (Figure 3). Specifically, these important regions are learnt using an offset network that takes input query features and returns corresponding offsets whose regions subsequently are used to sample candidates keys/values (Figure 3). In this work, we use this deformable attention to SSL for the first time, aiming to learn the association among feature embedding of 2D slices. We call this as Inter Deformable Attention and denote by f_{inter} . The f_{inter} contains N identical stacked layers. Each layer is composed of multi-head attention (MHA) layer followed by a simple feed-forward layer. Given an input tensor $Y \in \mathbb{R}^{D \times F_{\mathrm{in}}}$ added with a positional encoding to provide order information, the output of a single head h at each layer using deformable attention can be computed by the following step.

$$q^{(h)} = YW_q^h, \ \tilde{k}^{(h)} = \tilde{Y}W_k^h, \ \tilde{v}^{(h)} = \tilde{Y}W_v^h$$
 (6)

with
$$\tilde{Y}=\phi\left(Y;p+\Delta p\right),\;\Delta p=\theta_{\mathrm{offset}}\left(q^{(h)}\right)$$
 (7)

where W_q^h , W_k^h and $W_v^h \in \mathbb{R}^{F_{\mathrm{in}} \times d_h^v}$ are learned linear transformation that map the input Y to queries, keys, values respectively; θ_{offset} be the offset network that takes input as queries q^h and returns the offsets Δp ; $p \in \mathbb{R}^{D_G \times 2}$ denotes for the uniform grid of points with $D_G = D/r$ by a factor r to down-sample the grid size; finally $\phi(.;.)$ be a differentiable linear interpolation function used to sample important key/queries pairs inside predicted offsets.

We now compute the output of a deformable attention head \boldsymbol{h} as:

$$O^{(h)} = \sigma \left(q^{(h)} \tilde{k}^{(h)\top} / \sqrt{d^{(h)}} + \phi(\hat{B}; R) \right) \tilde{v}^{(h)}$$
 (8)

where $\sigma(.)$ denotes the softmax function, $d^{(h)}$ is the dimension of each head $h, \hat{B} \in \mathbb{R}^{(2D-1)}$ be a relative position bias matrix, R be the relative position offsets. More details on this bias matrix, we refer the readers to (Liu et al. 2021; Xia et al. 2022). The outputs of all heads (MHA) are aggregated by concatenating and projecting again as $\mathrm{MHA} = \mathrm{Concat}\left[O^{(1)},...,O^{(Nh)}\right]W^O$ where $W^O \in \mathbb{R}^{d_v \times d_v}$ is another learned linear transformation and Nh is the number of heads.

Given defined f_{inter} , we construct a 3D feature representation \mathbf{Z}_s for an augmented view $\mathbf{X}_s = \{\mathbf{x}_{1s}, \mathbf{x}_{2s}, ..., \mathbf{x}_{ns}\}$ of \mathbf{X} as follows. We denote by

$$\mathbf{Y} = \left[\{ f_{\text{intra}}(\mathbf{x}_{1s}) \}_{l=1}^{L}, \dots, \{ f_{\text{intra}}(\mathbf{x}_{ns}) \}_{l=1}^{L} \right]$$
 (9)

be the stacked input vectors with $\{f_{\text{intra}}(\mathbf{x}_{is})\}_{l=1}^L, \ i \in [1,n]$ indicates the multi-level features of image \mathbf{x}_{is} taken from the L last layers in f_{intra} . We then normalize the ouput of f_{inter} and obtain

$$\mathbf{Z_s} = f_{\text{inter}}(\mathbf{Y}) / ||f_{\text{inter}}(\mathbf{Y})||_2$$
 (10)

which is the holistic feature of \mathbf{X}_s . The embedding \mathbf{Z}_t for transformation $t \in T$ is computed analoguously. The clustering agreement for 3D volumes generalized from Eq.(3) can be defined as

$$L_{\text{inter}}(\mathbf{Z}_t, \mathbf{q}_t^{3D}, \mathbf{Z}_s, \mathbf{q}_s^{3D}) = l(\mathbf{Z}_t, \mathbf{q}_s^{3D}) + l(\mathbf{Z}_s, \mathbf{q}_t^{3D}) \quad (11)$$

where \mathbf{q}_s^{3D} , \mathbf{q}_t^{3D} are codes of \mathbf{Z}_s , \mathbf{Z}_t obtained by solving the matching problem in Eq.(2) where inputs are 3D augmented views' feature represents across 3D volumes $\mathbf{X_i}$ in a batch size $B \in \mathbb{D}$. Intuitively, two 3D features \mathbf{Z}_s and \mathbf{Z}_t should be identical in their cluster assignments. Finally, by minimizing over samples in \mathbb{D} , we jointly learn both f_{intra} , f_{inter} and \mathbf{C} through

$$L_{3D} = \min_{f_{\text{intra}}, \mathbf{C}, f_{\text{inter}}} E_{\mathbf{X} \in \mathbb{D}} \left[L_{\text{inter}}(\mathbf{Z}_t, \mathbf{q}_t^{3D}, \mathbf{Z}_s, \mathbf{q}_s^{3D}) \right]$$
with $s, t \sim T$. (12)

Setting	Pre-Training Data	Modality	Num
	LUNA2016	3D CT	623
Universal	LiTS2017	3D CT	111
	BraTS2018	3D MRI	760
	MSD (Heart)	3D MRI	30
	MOTS	3D CT	936
Unified	LIDC-IDRI	3D CT	1008
	RibFrac	3D CT	420
	TCIA-CT	3D CT	1300
	NIH ChestX-ray8	2D X-ray	108948

Table 1: Overview pre-training settings in our experiment. The *Universal* setting uses four unlabeled 3D datasets while *Unified* uses six unlabeled datasets including mixed 2D and 3D modalities.

Masked Feature Embedding Prediction

To enhance long-term dependence learning of f_{inter} , we additionally introduce a new SSL proxy task inspired by the BERT language model (Devlin et al. 2018). Given a set of 2D slice embedding vectors \mathbf{Y} in Eq.(9) obtained from $\mathbf{X_s}$ ($\mathbf{X} \in \mathbb{D}, s \sim T$), we dynamically mask some inputs $\{f_{\text{intra}}(\mathbf{x}_{is})\}_{l=1}^L, i \in [1, n]$ and ask the *Inter Deformable Attention* to predict missing encoding vectors given the unmasked embedding vectors. To do this, we define a binary vector $\mathbf{m} = (m_1, \ldots, m_n)$ of length n where $m_i = 1$ indicate the input i-th of \mathbf{Y} will be masked and 0 otherwise. The input for SSL task then is defined as:

$$\mathbf{m} \odot \mathbf{Y} = \begin{cases} [\text{MASK}], \ m_i = 1\\ \{f_{\text{intra}}(\mathbf{x}_{is})\}_{l=1}^L, \ m_i = 0 \end{cases}$$
 (13)

where MASK is a learnable parameter during the training step. We denote by $f_{\rm decode}$, a fully connected layer, that takes the outputs of $f_{\rm inter}$ and predicts masked vectors. For each ${\bf m}$, we randomly assign $m_i=1$ for 10% of ${\bf m}$. The output of $f_{\rm decode}$ at each masked ${\bf y}_i$ is:

$$\mathbf{y}_i = \mathbf{W_d} \mathbf{h}_i^N + \mathbf{b}_i$$
, where $m_i = 1$. (14)

with $\mathbf{W}_d \in \mathbb{R}^{F_{in} \times F_D}$ and $\mathbf{b}_i \in \mathbb{R}^{F_{in}}$ are fully-connected layers and biases respectively. The masked feature embedding prediction is defined as:

$$L_{mask} = \min_{\substack{f_{\text{inter}} \\ f_{\text{decode}}}} E_{\mathbf{x} \in \mathbb{D}} \left[\sum_{i:m_i=1} ||f_{\text{intra}}(\mathbf{x}_{is}) - f_{\text{decode}}(f_{\text{inter}}(\mathbf{m} \odot \mathbf{Y}))||_2 \right]$$
(15)

Experiment Results

Data and Baseline Setup

Pre-training and Downstream Tasks We describe the details of datasets used for pre-training and downstream tasks in Table 1 and Table 2, respectively. In summary, there are thirteen datasets comprising LUNA2016 (Setio et al.

2015), LiTS2017 (Bilic et al. 2019), BraTS2018 (Bakas et al. 2018), MSD (Heart) (Simpson et al. 2019), MOTS (Zhang et al. 2021), LIDC-IDRI (Clark et al. 2013; Armato III et al. 2011), RibFrac (Jin et al. 2020), TCIA-CT (Clark et al. 2013; Harmon et al. 2020), NIH ChestX-ray8 (Wang et al. 2017), MMWHS-CT/MMWHS-MRI (Zhuang and Shen 2016), VinDR-CXR (Nguyen et al. 2022c), and JSRT (Shiraishi et al. 2000; Van Ginneken, Stegmann, and Loog 2006). In pre-training settings, we mainly evaluate in two scenarios, namely Universal and Unified following prior works of Zhang et al. (2020) and Xie et al. (2021), respectively. However, we cannot access the dataset called "Tianchi dataset" in *Unified* setting thus we only train with five remaining datasets. The downstream tasks are conducted in three contexts with diverse applications as described Table 2. For objective assessment, we use Intersection over Union (IoU) computed on 3D data for segmentation, Area Under the Curve (AUC) for 3D classification, Dice coefficient scores for 2D segmentation, and Average Precision with IoU=0.5 for multi-object detection.

Pre-training	Testing Data	Task
Seen Domain in <i>Universal</i>	BraTS2018 LUNA 2016	3D MRI segmentation 3D CT classification
Unseen Domain in <i>Universal</i>	MMWHS-CT MMWHS-MRI VinDR-CXR	3D CT segmentation 3D MRI segmentation 2D X-ray detection
Unseen Domain in <i>Unified</i>	JSRT	2D X-ray segmentation

Table 2: Overview downstream tasks used in our experiment. *Seen Domain* indicates for downstream tasks where the training data was used in the pre-training step without labels, *Unseen Domain* means that datasets in pre-training and downstream are different.

Competing Algorithms We implement variations of DeepCluster and SwAV based the proposed method and compare with the following approaches:

- 2D SSL methods: SimCLR (Chen et al. 2020a), PGL (Xie et al. 2020), Moco-v2 (Chen et al. 2020b), Deep-Cluster-v2 (Caron et al. 2020), SwAV (Caron et al. 2020), Barlow-Twins (Zbontar et al. 2021), Moco-V3 (Chen, Xie, and He 2021), PCRL (Zhou et al. 2021a), and DINO (Caron et al. 2021). Both Moco-v3 and DINO use Pyramid Transformer Unet (Xie et al. 2021) as backbone.
- 3D SSL methods: 3D Rotation, 3D JigSaw (Taleb et al. 2020), Universal Model (Zhang et al. 2020), Models Genesis (Zhou et al. 2021b), TransVW (Haghighi et al. 2021), SwinViT3D (Tang et al. 2022), and our two implementations for the 3D case of DeepCluster-v2 and SwAV, namely 3D-DeepCluster and 3D-SwAV.
- 2D/3D supervised pre-trained methods: 2D pre-trained ImageNet (He et al. 2016), I3D (Carreira and Zisserman 2017), NiftyNet (Gibson et al. 2018), and Med3D (Chen, Ma, and Zheng 2019).

• Other methods: training from scratch for 2D or 3D using ResNet-50, V-Net architecture (Milletari, Navab, and Ahmadi 2016), 3D-Transformer (Hatamizadeh et al. 2022), Pyramid Transformer Unet (PTU) (Xie et al. 2021) and finally USST (Xie et al. 2021), a joint 2D and 3D approach similar to ours.

Most baseline results are taken from (Zhang et al. 2020) and (Xie et al. 2021). With LUNA2016 dataset, we use the latest ground-truth, denoted as LUNA2016-v2, and provide results obtained when training with batch sizes of 8, 16, 32, each with two trial times. For new competitors, we describe experiment setups in the appendix. In short, for 2D self-supervised methods (ResNet-50 backbone) such as Moco-v2 or Barlow-Twins, we extract all 2D slices from 3D volumes in pre-training data and train SSL tasks with 100 epochs. With state-of-the-art 3D SSL methods TransVW and Swin-ViT3D, we download pre-trained weights and use published implementation to fine-tune as author's suggestions. For two our implementations of 3D-DeepCluster and 3D-SwAV, we train with all 3D data of *Universal* in pre-training step.

Method	BraTS2018	LUNA2016-v2
Scratch (3D)	58.51 ± 2.61	94.15 ± 3.97
V-Net	59.01 ± 2.59	95.85 ± 1.09
3D-Transformer	66.54 ± 0.40	85.15 ± 2.62
I3D	67.83 ± 0.75	92.43 ± 2.63
NiftyNet	60.78 ± 1.60	94.16 ± 1.52
Med3D	66.09 ± 1.35	91.32 ± 1.47
3D-Rotation	56.48 ± 1.78	95.91 ± 1.26
3D-JigSaw	59.65 ± 0.81	89.12 ± 1.71
Models Genesis	67.96 ± 1.29	92.46 ± 5.54
Universal Model	72.10 ± 0.67	N/A
3D-DeepCluster	59.20 ± 1.69	89.03 ± 2.56
3D-SwAV	62.81 ± 1.03	88.79 ± 5.48
TransVW	68.82 ± 0.38	93.84 ± 6.73
SwinViT3D	70.58 ± 1.27	88.68 ± 2.63
Scratch (2D)	66.82 ± 1.32	N/A
Pre-trained ImageNet	71.24 ± 2.30	N/A
SimCLR	70.37 ± 1.11	N/A
Moco-v2	70.82 ± 0.22	N/A
Barlow-Twins	67.35 ± 0.55	N/A
Deep-Cluster-v2	69.21 ± 2.10	N/A
SwAV	69.83 ± 2.44	N/A
Our (DeepCluster-v2)	72.81 ± 0.15	93.91 ± 0.67
Our (SwAV)	$\underline{73.03} \pm 0.42$	94.22 ± 1.11

Table 3: Comparing SSL approaches on *Seen Domains* trained on the *Universal setting* for BraTS2018 (MRI - segmentation) and LUNA2016-v2 (CT - classification). We categorize the methods into three sub-groups from top to bottom: 3D, 2D, and combined 2D-3D SSL methods. Two top results in 2D or combined 2D-3D SSL data are boldfaced and italicized. The best values overall are underlined. N/A indicates pre-trained models that are unable to transfer (Universal Model's results are not available in LUNA2016-v2).

Implementation Details

Pre-training Our method is trained in three stages. Stage 1 learns f_{intra} using Eq. (5) with 100 epochs using batch size

Method	MMWHS (CT)	MMWHS (MRI)
Scratch (3D)	68.29 ± 1.68	67.04 ± 2.18
V-Net	69.66 ± 3.65	67.50 ± 3.76
3D-Transformer	67.30 ± 2.29	67.64 ± 2.21
I3D	76.63 ± 2.32	66.71 ± 1.27
Nifty Net	74.91 ± 2.78	64.60 ± 1.96
Med3D	75.01 ± 0.74	63.43 ± 0.61
3D Rotation	67.54 ± 2.80	71.36 ± 1.70
3D Jigsaw	68.40 ± 2.92	72.99 ± 2.54
Model Geneis	76.48 ± 2.89	74.53 ± 1.69
Universal Model	78.14 ± 0.77	77.52 ± 0.50
3D-DeepCluster	69.47 ± 1.44	75.83 ± 2.29
3D-SwAV	69.90 ± 1.31	69.41 ± 1.93
TransVW	79.74 ± 2.78	75.08 ± 2.04
SwinViT3D	70.19 ± 1.23	78.25 ± 1.66
Scratch (2D)	74.25 ± 2.05	52.34 ± 4.31
Pre-trained ImageNet	73.49 ± 3.15	72.66 ± 2.46
SimCLR	78.56 ± 2.12	72.72 ± 1.29
Moco-v2	80.25 ± 0.93	71.85 ± 1.25
Barlow-Twins	80.95 ± 2.47	70.90 ± 1.89
Deep-Cluster-v2	81.03 ± 1.17	74.51 ± 1.92
SwAV	82.15 ± 1.19	74.50 ± 1.20
Our (DeepCluster-v2)	83.58 ± 1.54	78.14 ± 1.32
Our (SwAV)	$\underline{84.89} \pm 0.68$	$\underline{78.73} \pm 1.21$

Table 4: Comparing SSL approaches on *Unseen Domains* trained on the *Universal setting* for the segmentation task in MMWHS dataset (both CT and MRI). We categorize the methods into three sub-groups from top to bottom: 3D, 2D, and combined 2D-3D SSL methods. Two top results in 2D or combined 2D-3D SSL data are boldfaced and italicized. The best values overall are underlined.

of 1024 images, Stage 2 learns $f_{\rm inter}$ using Eq. (15) with 100 epochs using batch size of 12 volumes, and Stage 3 learns for both $f_{\rm intra}, f_{\rm inter}$ using Eq. (12) also with 100 epochs and batch size of 12 volumes.

We use ResNet-50 as the backbone for 2D feature extractor $f_{\rm intra}$. The features for each image are concatenated from five blocks of ResNet-50. The architecture of $f_{\rm inter}$ has four pyramid structure blocks composed from deformable attention (Eq. (8)). Details for these configurations can be found in Appendix. In the *Universal* or *Unified* setting, we utilize all 3D data as benchmarks and further extract 2D slices from them to train $f_{\rm intra}$ in Stage 1. All experiments are conducted on a A100-GPU system with 4 GPUs, 40GB of memory each with Pytorch. It takes in average 30 hours to finish the pre-training step.

Downstream Task we use the SGD with a learning rate selected in a set $\{0.1, 0.01\}$ and select a specific number of epoch depended on downstream task properties (Appendix). The results are reported by running training-testing five times and computing the average values (except LUNA2016-v2 dataset). For the 2D/3D segmentation task, we use the pre-trained 2D-CNN feature extractor in each 2D baseline ($f_{\rm intra}$ in our method) as the network backbone of a 2D U-net (Ronneberger, Fischer, and Brox 2015). This net-

Method	VinDr-CXR (X-ray - Detect.)	
All 3D CNN-based methods	N/A	
Scratch (2D) Pre-trained ImageNet SimCLR Moco-v2 Barlow-Twins Deep-Cluster-v2 SwAV	24.35 ± 0.04 27.82 ± 0.29 26.87 ± 0.32 27.20 ± 0.66 26.83 ± 0.13 28.03 ± 0.41 27.70 ± 0.22	
Our (DeepCluster-v2) Our (SwAV)	28.47 ± 0.40 27.47 ± 0.18	

Table 5: Comparing SSL approaches on *Unseen Domains* trained on the *Universal setting* for the VinDr-CXR dataset (X-ray - abnormal chest detection). We categorize the methods into three sub-groups from top to bottom: 3D, 2D, and combined 2D-3D SSL methods. Two top results overall are boldfaced and italicized. N/A indicates pre-trained models that are unable to transfer.

work is trained with cross-entropy and dice loss. We predict segmentation at each 2D slice and merge results for 3D volumes. The 3D classification is solved by building on top of the deformable transformer two fully-connected layers and fine-tuning for both $f_{\rm inter}$ and $f_{\rm intra}$ with the cross-entropy loss. For the 2D object detection task (VinDr-CXR), we use the 2D-CNN feature extractor ($f_{\rm intra}$) as the backbone of Faster R-CNN model (Ren et al. 2015).

Performance Evaluation

Dimension-specific vs. Cross-dimension Pre-training Tables 3 indicates that 2D CNN based-models cannot transfer to the 3D lung node classification task in LUNA2016-v2 (denoted N/A) given input 3D volumes. Likewise, due to data compatibility issues, 3D CNN-based methods cannot apply for abnormal chest detection in X-ray, as shown in Table 5. In contrast, our models pre-trained on several medical datasets can be transferred successfully in both cases due to the hybrid CNN-Transformer architecture. We argue that such property is one of the most valuable points of this study.

As compared with plain 2D-SwAV, DeepCluster-V2, and their extended versions with 3D CNN, namely 3D-SwAV and 3D-DeepCluster, we show a significant improvement in several settings, especially for segmentation tasks (Tables 3,4). For instance, a gain performance of 2-3% on average on BraTS, MMWHS-CT/MRI datasets. Furthermore, we also achieve better accuracy on 3D classification and 2D object detection, although with smaller margins. In conclusion, this analysis shows that exploiting deformable self-attention in conjunction with 2D CNN to model 3D volume features in our framework is a promising approach.

Comparison to SOTA Methods and Visualizations In the Universal setting, except the LUNA2016-v2 case where we are third, our methods based on DeepCluster-V2 or SwAV hold the best records on BraTS, MMWHS-CT/MRI

Methods	Backbone	JSRT (X-ray, seg.)		
Methous		20%	40%	100%
Scratch CNN	RN50	84.05	87.63	90.96
Scratch PTU	Trans.	85.55	88.83	91.22
Pre-trained ImageNet	RN50	87.90	90.01	91.73
Moco-v2	RN50	88.65	91.03	92.32
PGL	RN50	89.01	91.39	92.76
PCRL	RN50	89.55	91.53	93.07
Moco-v3	Trans.	90.07	91.75	92.68
DINO	Trans.	90.40	92.16	93.03
USST	Trans.	91.88	93.15	94.08
Our (DeepC-v2)	RN50	90.60	92.87	94.31
Our (SwAV)	RN50	89.98	93.03	94.45

Table 6: Performance comparison on the 2D X-ray JSRT segmentation tasks using different SSL approaches trained on the *Unified* setting. We categorize the methods into two sub-groups from top to bottom: 2D and combined 2D-3D SSL methods. For backbone, "RN50" and "Trans" mean ResNet-50 and Transformer architectures, respectively. Two top results are boldfaced and italicized.

segmentation tasks compared with remaining baselines, especially with cutting edges 3D-SSL methods as Universal Model, TransVW or SwinViT3D (using Swin Transformer). With the VinDr-CXR detection task, we continue to reach the best rank, followed by the plane 2D DeepCluster-v2 though with smaller margins. In the Unified setting (Table 6), we also surpass competitors (100% data), especially with USST, a method using Pyramid Vision Transformer trained on mixed 2D and 3D data. However, USST works better than us when decreasing training data to 40% and 20%. We consider this as a potential limitation that needs to improve. Though it's worth noting that we could not access all data as USST in the pre-training step, as shown in Table 1. For visualization, we provide a typical example of multi-modal heart segmentation for MMWHS-CT in Figure 4.

Computational Complexity and Ablation Study We compare the total parameters with top baselines and methods using Transformer in Table 8. In short, our total parameter is half of the SwinViT3D but we attain better performance in overall. The contributions of proposed SSL tasks and multilevel features are presented in Table 7, where all components contribute to accurate overall growth.

Setting	CT	MRI
W/o mask prediction	82.53	77.35
W/o 3D clustering	81.97	76.18
Full model	84.89	78.73
Full model w/o multi-feature	83.56	78.12

Table 7: Ablation studies for the SwAV on heart segmentation for the MMWHS-CT and MMWHS-MRI datasets.

Method	#Param
SwinViT3D	62.19 M
TransVW	19.7 M
Universal Model	19.7 M
USST	$47.8\mathrm{M}$
Our	31.16 M

Table 8: Computational complexity of top baselines and transformer-based methods. For USST, we follow general descriptions in paper to re-configure architecture.

Ground-truth	Deep-Cluster-v2 (Our)	Deep-Cluster-v2 (Baseline)	SwAV (Our)	SwAV (Baseline)

Figure 4: Heart structure segmentation on MMWHS-CT. The figures show that baselines tend to over-segment in the first row while generating noise regions in the second row. On the contrary, our methods produce more precise results.

Conclusion

We contribute to the self-supervised learning medical imaging literature a new approach that is efficient in using numerous unlabeled data types and be flexible with data dimension barriers in downstream tasks. To that end, we developed a deformable self-attention mechanism on top of a 2D CNN architecture, which leads to both intra- and inter-correlations formed in our framework. Furthermore, our two novel SSL tasks including 3D agreement clustering and masked embedding predictions impose a tighter constraint in learning feature space, advancing pre-trained network performance in a variety of medical tasks. In the future, we will investigate this method for various SSL approaches, aiming to validate its universality and robustness in real-life medical usage.

Acknowledgements

This research has been supported by the pAItient project (BMG, 2520DAT0P2), Ophthalmo-AI project (BMBF, 16SV8639) and the Endowed Chair of Applied Artificial Intelligence, Oldenburg University. Binh T. Nguyen wants to thank AISIA Lab, University of Science, and Vietnam National University in Ho Chi Minh City for their support.

References

Armato III, S. G.; McLennan, G.; Bidaut, L.; McNitt-Gray, M. F.; Meyer, C. R.; Reeves, A. P.; Zhao, B.; Aberle, D. R.; Henschke, C. I.; Hoffman, E. A.; et al. 2011. The lung image database consortium (LIDC) and image database resource initiative (IDRI): a completed reference database of lung nodules on CT scans. *Medical physics*, 38(2): 915–931.

- Bakas, S.; Reyes, M.; Jakab, A.; Bauer, S.; Rempfler, M.; Crimi, A.; Shinohara, R. T.; Berger, C.; Ha, S. M.; Rozycki, M.; et al. 2018. Identifying the best machine learning algorithms for brain tumor segmentation, progression assessment, and overall survival prediction in the BRATS challenge. *arXiv:1811.02629*.
- Bilic, P.; Christ, P. F.; Vorontsov, E.; Chlebus, G.; Chen, H.; Dou, Q.; Fu, C.-W.; Han, X.; Heng, P.-A.; Hesser, J.; et al. 2019. The liver tumor segmentation benchmark (LiTS). *arXiv:1901.04056*.
- Caron, M.; Bojanowski, P.; Joulin, A.; and Douze, M. 2018. Deep clustering for unsupervised learning of visual features. In *Proceedings of the European conference on computer vision (ECCV)*, 132–149.
- Caron, M.; Misra, I.; Mairal, J.; Goyal, P.; Bojanowski, P.; and Joulin, A. 2020. Unsupervised learning of visual features by contrasting cluster assignments. *Neural Information Processing Systems (NeurIPS)*.
- Caron, M.; Touvron, H.; Misra, I.; Jégou, H.; Mairal, J.; Bojanowski, P.; and Joulin, A. 2021. Emerging properties in self-supervised vision transformers. In *Proceedings of the IEEE/CVF International Conference on Computer Vision*, 9650–9660.
- Carreira, J.; and Zisserman, A. 2017. Quo vadis, action recognition? A new model and the kinetics dataset. In *proceedings of the IEEE Conference on Computer Vision and Pattern Recognition*, 6299–6308.
- Chaitanya, K.; Erdil, E.; Karani, N.; and Konukoglu, E. 2020. Contrastive learning of global and local features for medical image segmentation with limited annotations. *Advances in Neural Information Processing Systems*, 33: 12546–12558.
- Chen, L.; Bentley, P.; Mori, K.; Misawa, K.; Fujiwara, M.; and Rueckert, D. 2019. Self-supervised learning for medical image analysis using image context restoration. *Medical image analysis*, 58: 101539.
- Chen, S.; Ma, K.; and Zheng, Y. 2019. Med3d: Transfer learning for 3d medical image analysis. *arXiv:1904.00625*.
- Chen, T.; Kornblith, S.; Norouzi, M.; and Hinton, G. 2020a. A simple framework for contrastive learning of visual representations. In *International conference on machine learning*, 1597–1607. PMLR.
- Chen, X.; Fan, H.; Girshick, R.; and He, K. 2020b. Improved baselines with momentum contrastive learning. *arXiv:2003.04297*.
- Chen, X.; Xie, S.; and He, K. 2021. An empirical study of training self-supervised vision transformers. In *Proceedings of the IEEE/CVF International Conference on Computer Vision*, 9640–9649
- Cheplygina, V.; de Bruijne, M.; and Pluim, J. P. 2019. Not-so-supervised: a survey of semi-supervised, multi-instance, and transfer learning in medical image analysis. *Medical image analysis*, 54: 280–296.
- Clark, K.; Vendt, B.; Smith, K.; Freymann, J.; Kirby, J.; Koppel, P.; Moore, S.; Phillips, S.; Maffitt, D.; Pringle, M.; et al. 2013. The Cancer Imaging Archive (TCIA): maintaining and operating a public information repository. *Journal of digital imaging*, 26(6): 1045–1057.
- Deng, J.; Dong, W.; Socher, R.; Li, L.-J.; Li, K.; and Fei-Fei, L. 2009. Imagenet: A large-scale hierarchical image database. In 2009 IEEE conference on computer vision and pattern recognition, 248–255. Ieee.
- Devlin, J.; Chang, M.-W.; Lee, K.; and Toutanova, K. 2018. Bert: Pre-training of deep bidirectional transformers for language understanding. *arXiv*:1810.04805.

- Do, K.; Tran, T.; and Venkatesh, S. 2021. Clustering by maximizing mutual information across views. In *Proceedings of the IEEE/CVF International Conference on Computer Vision*, 9928–9938
- Dosovitskiy, A.; Beyer, L.; Kolesnikov, A.; Weissenborn, D.; Zhai, X.; Unterthiner, T.; Dehghani, M.; Minderer, M.; Heigold, G.; Gelly, S.; et al. 2020. An image is worth 16x16 words: Transformers for image recognition at scale. *arXiv preprint arXiv:2010.11929*.
- Gibson, E.; Li, W.; Sudre, C.; Fidon, L.; Shakir, D. I.; Wang, G.; Eaton-Rosen, Z.; Gray, R.; Doel, T.; Hu, Y.; et al. 2018. NiftyNet: a deep-learning platform for medical imaging. *Computer methods and programs in biomedicine*, 158: 113–122.
- Haghighi, F.; Taher, M. R. H.; Zhou, Z.; Gotway, M. B.; and Liang, J. 2021. Transferable visual words: Exploiting the semantics of anatomical patterns for self-supervised learning. *IEEE transactions on medical imaging*, 40(10): 2857–2868.
- Harmon, S. A.; Sanford, T. H.; Xu, S.; Turkbey, E. B.; Roth, H.; Xu, Z.; Yang, D.; Myronenko, A.; Anderson, V.; Amalou, A.; et al. 2020. Artificial intelligence for the detection of COVID-19 pneumonia on chest CT using multinational datasets. *Nature communications*, 11(1): 1–7.
- Hatamizadeh, A.; Tang, Y.; Nath, V.; Yang, D.; Myronenko, A.; Landman, B.; Roth, H. R.; and Xu, D. 2022. Unetr: Transformers for 3d medical image segmentation. In *Proceedings of the IEEE/CVF Winter Conference on Applications of Computer Vision*, 574–584.
- He, K.; Fan, H.; Wu, Y.; Xie, S.; and Girshick, R. 2020. Momentum contrast for unsupervised visual representation learning. In *Proceedings of the IEEE/CVF Conference on Computer Vision and Pattern Recognition*, 9729–9738.
- He, K.; Zhang, X.; Ren, S.; and Sun, J. 2016. Deep residual learning for image recognition. In *Proceedings of the IEEE conference on computer vision and pattern recognition*, 770–778.
- Jin, L.; Yang, J.; Kuang, K.; Ni, B.; Gao, Y.; Sun, Y.; Gao, P.; Ma, W.; Tan, M.; Kang, H.; et al. 2020. Deep-learning-assisted detection and segmentation of rib fractures from CT scans: Development and validation of FracNet. *EBioMedicine*, 62: 103106.
- Jun, E.; Jeong, S.; Heo, D.-W.; and Suk, H.-I. 2021. Medical transformer: Universal brain encoder for 3D MRI analysis. *arXiv* preprint arXiv:2104.13633.
- Kaissis, G. A.; Makowski, M. R.; Rückert, D.; and Braren, R. F. 2020. Secure, privacy-preserving and federated machine learning in medical imaging. *Nature Machine Intelligence*, 2(6): 305–311.
- Li, J.; Zhou, P.; Xiong, C.; and Hoi, S. C. 2021. Prototypical contrastive learning of unsupervised representations. *International Conference on Learning Representations (ICLR)*.
- Liu, Z.; Lin, Y.; Cao, Y.; Hu, H.; Wei, Y.; Zhang, Z.; Lin, S.; and Guo, B. 2021. Swin transformer: Hierarchical vision transformer using shifted windows. In *Proceedings of the IEEE/CVF International Conference on Computer Vision*, 10012–10022.
- Milletari, F.; Navab, N.; and Ahmadi, S.-A. 2016. V-net: Fully convolutional neural networks for volumetric medical image segmentation. In 2016 fourth international conference on 3D vision (3DV), 565–571. IEEE.
- Nguyen, D.; Nguyen, D. M.; Vu, H.; Nguyen, B. T.; Nunnari, F.; and Sonntag, D. 2021. An attention mechanism using multiple knowledge sources for COVID-19 detection from CT images. In *The Thirty-Fifth AAAI Conference on Artificial Intelligence (AAAI-2021), Workshop: Trustworthy AI for Healthcare*, volume 360.

- Nguyen, D. H.; Nguyen, D. M.; Mai, T. T.; Nguyen, T.; Tran, K. T.; Nguyen, A. T.; Pham, B. T.; and Nguyen, B. T. 2022a. ASMCNN: An efficient brain extraction using active shape model and convolutional neural networks. *Information Sciences*, 591: 25–48.
- Nguyen, D. M.; Nguyen, T. T.; Vu, H.; Pham, Q.; Nguyen, M.-D.; Nguyen, B. T.; and Sonntag, D. 2022b. TATL: task agnostic transfer learning for skin attributes detection. *Medical Image Analysis*, 102359.
- Nguyen, H. Q.; Lam, K.; Le, L. T.; Pham, H. H.; Tran, D. Q.; Nguyen, D. B.; Le, D. D.; Pham, C. M.; Tong, H. T.; Dinh, D. H.; et al. 2022c. Vindr-cxr: An open dataset of chest x-rays with radiologist's annotations. *Scientific Data*, 9(1): 1–7.
- Pan, E.; and Kang, Z. 2021. Multi-view contrastive graph clustering. *Advances in neural information processing systems*, 34: 2148–2159.
- Raghu, M.; Zhang, C.; Kleinberg, J.; and Bengio, S. 2019. Transfusion: Understanding transfer learning for medical imaging. *Advances in neural information processing systems*, 32.
- Ren, S.; He, K.; Girshick, R.; and Sun, J. 2015. Faster r-cnn: Towards real-time object detection with region proposal networks. *Advances in neural information processing systems*, 28.
- Ronneberger, O.; Fischer, P.; and Brox, T. 2015. U-net: Convolutional networks for biomedical image segmentation. In *International Conference on Medical image computing and computer-assisted intervention*, 234–241. Springer.
- Setio, A. A.; Jacobs, C.; Gelderblom, J.; and van Ginneken, B. 2015. Automatic detection of large pulmonary solid nodules in thoracic CT images. *Medical physics*, 42(10): 5642–5653.
- Shiraishi, J.; Katsuragawa, S.; Ikezoe, J.; Matsumoto, T.; Kobayashi, T.; Komatsu, K.-i.; Matsui, M.; Fujita, H.; Kodera, Y.; and Doi, K. 2000. Development of a digital image database for chest radiographs with and without a lung nodule: receiver operating characteristic analysis of radiologists' detection of pulmonary nodules. *American Journal of Roentgenology*, 174(1): 71–74.
- Simpson, A. L.; Antonelli, M.; Bakas, S.; Bilello, M.; Farahani, K.; Van Ginneken, B.; Kopp-Schneider, A.; Landman, B. A.; Litjens, G.; Menze, B.; et al. 2019. A large annotated medical image dataset for the development and evaluation of segmentation algorithms. *arXiv:1902.09063*.
- Taleb, A.; Loetzsch, W.; Danz, N.; Severin, J.; Gaertner, T.; Bergner, B.; and Lippert, C. 2020. 3d self-supervised methods for medical imaging. *Advances in Neural Information Processing Systems*, 33: 18158–18172.
- Tang, Y.; Yang, D.; Li, W.; Roth, H. R.; Landman, B.; Xu, D.; Nath, V.; and Hatamizadeh, A. 2022. Self-supervised pre-training of swin transformers for 3d medical image analysis. In *Proceedings of the IEEE/CVF Conference on Computer Vision and Pattern Recognition*, 20730–20740.
- Van Ginneken, B.; Stegmann, M. B.; and Loog, M. 2006. Segmentation of anatomical structures in chest radiographs using supervised methods: a comparative study on a public database. *Medical image analysis*, 10(1): 19–40.
- Vaswani, A.; Shazeer, N.; Parmar, N.; Uszkoreit, J.; Jones, L.; Gomez, A. N.; Kaiser, Ł.; and Polosukhin, I. 2017. Attention is all you need. In *Advances in neural information processing systems*, 5998–6008.
- Wang, D.; Zhang, Y.; Zhang, K.; and Wang, L. 2020. Focalmix: Semi-supervised learning for 3d medical image detection. In *Proceedings of the IEEE/CVF Conference on Computer Vision and Pattern Recognition*, 3951–3960.

- Wang, W.; Xie, E.; Li, X.; Fan, D.-P.; Song, K.; Liang, D.; Lu, T.; Luo, P.; and Shao, L. 2021. Pyramid vision transformer: A versatile backbone for dense prediction without convolutions. In *Proceedings of the IEEE/CVF International Conference on Computer Vision*, 568–578.
- Wang, X.; Peng, Y.; Lu, L.; Lu, Z.; Bagheri, M.; and Summers, R. M. 2017. Chestx-ray8: Hospital-scale chest x-ray database and benchmarks on weakly-supervised classification and localization of common thorax diseases. In *Proceedings of the IEEE conference on computer vision and pattern recognition*, 2097–2106.
- Wu, Z.; Xiong, Y.; Yu, S. X.; and Lin, D. 2018. Unsupervised feature learning via non-parametric instance discrimination. In *Proceedings of the IEEE conference on computer vision and pattern recognition*, 3733–3742.
- Xia, Z.; Pan, X.; Song, S.; Li, L. E.; and Huang, G. 2022. Vision transformer with deformable attention. In *Proceedings of the IEEE/CVF Conference on Computer Vision and Pattern Recognition*, 4794–4803.
- Xie, Y.; Zhang, J.; Liao, Z.; Xia, Y.; and Shen, C. 2020. PGL: prior-guided local self-supervised learning for 3D medical image segmentation. *arXiv* preprint arXiv:2011.12640.
- Xie, Y.; Zhang, J.; Xia, Y.; and Wu, Q. 2021. Unified 2D and 3D Pre-training for Medical Image classification and Segmentation. *arXiv preprint arXiv:2112.09356*.
- Zbontar, J.; Jing, L.; Misra, I.; LeCun, Y.; and Deny, S. 2021. Barlow twins: Self-supervised learning via redundancy reduction. *arXiv:2103.03230*.
- Zhang, J.; Xie, Y.; Xia, Y.; and Shen, C. 2021. DoDNet: Learning to segment multi-organ and tumors from multiple partially labeled datasets. In *Proceedings of the IEEE/CVF Conference on Computer Vision and Pattern Recognition*, 1195–1204.
- Zhang, X.; Zhang, Y.; Zhang, X.; and Wang, Y. 2020. Universal Model for 3D Medical Image Analysis. *CoRR*, abs/2010.06107.
- Zhou, H.-Y.; Lu, C.; Yang, S.; Han, X.; and Yu, Y. 2021a. Preservational learning improves self-supervised medical image models by reconstructing diverse contexts. In *Proceedings of the IEEE/CVF International Conference on Computer Vision*, 3499–3509.
- Zhou, Z.; Sodha, V.; Pang, J.; Gotway, M. B.; and Liang, J. 2021b. Models genesis. *Medical image analysis*, 67: 101840.
- Zhu, X.; Su, W.; Lu, L.; Li, B.; Wang, X.; and Dai, J. 2020. Deformable detr: Deformable transformers for end-to-end object detection. *arXiv preprint arXiv:2010.04159*.
- Zhuang, X.; Li, Y.; Hu, Y.; Ma, K.; Yang, Y.; and Zheng, Y. 2019. Self-supervised feature learning for 3d medical images by playing a rubik's cube. In *International Conference on Medical Image Computing and Computer-Assisted Intervention*, 420–428. Springer.
- Zhuang, X.; and Shen, J. 2016. Multi-scale patch and multi-modality atlases for whole heart segmentation of MRI. *Medical image analysis*, 31: 77–87.